

HIGH-VELOCITY BIPOLAR OUTFLOW AND DISKLIKE ENVELOPE IN THE CARBON STAR V HYDRAE

NAOMI HIRANO,¹ HIROKO SHINNAGA,² DINH-V-TRUNG,¹ DAVID FONG,² ERIC KETO,³ NIMESH PATEL,³
CHUNHUA QI,³ KEN YOUNG,³ QIZHOU ZHANG,³ AND JUNHUI ZHAO³

Received 2004 May 1; accepted 2004 July 14; published 2004 October 28

ABSTRACT

Using the partially completed Submillimeter Array with five antennas, we have observed the CO $J = 2-1$ and $3-2$ emission from the envelope surrounding the carbon star V Hya. The high angular resolution ($2''-4''$) maps show that V Hya is powering a bipolar molecular jet with an extreme velocity of $70-185 \text{ km s}^{-1}$. The axis of this high-velocity jet is perpendicular to the major axis of the flattened disklike envelope, which is expanding with a velocity of $\sim 16 \text{ km s}^{-1}$. There is a third kinematic component, a medium-velocity wind with a deprojected velocity of $40-120 \text{ km s}^{-1}$ moving along the disk plane. Both the high-velocity jet and the medium-velocity wind have a dynamical timescale of a few hundred years. The flattened structure and the collimated jet observed in V Hya suggest that the formation of asymmetrical structure proceeds while the central star is still in the asymptotic giant branch phase.

Subject headings: ISM: individual (V Hydrae) — ISM: jets and outflows — ISM: molecules — stars: AGB and post-AGB

1. INTRODUCTION

V Hya, an evolved star located 380 pc away from the Sun (Knapp et al. 1997), is a carbon star with a high mass loss. Although the optical properties of V Hya are those of a normal N-type carbon star, the envelope surrounding this star shows several peculiar properties. Single-dish molecular line observations have shown that the envelope of V Hya is elongated along the north-south direction with a velocity gradient along its minor axis (e.g., Kahane et al. 1996). Such morphological and kinematical properties differ from those of the typical asymptotic giant branch (AGB) envelope, which has a spherically symmetric shape and uniform expansion. In addition, V Hya is associated with a very fast ($>100 \text{ km s}^{-1}$) outflow that was observed in optical and infrared spectra (e.g., Sahai & Wannier 1988; Lloyd Evans 1991) and in CO $J = 2-1$ and $3-2$ spectra (Knapp et al. 1997). Knapp et al. (1997) also found that the high-velocity CO gas is bipolar and proposed that the fast-moving gas is expanding along the east-west direction, perpendicular to the major axis of the envelope. However, previous observations did not bring us detailed structure of the high-velocity outflow and the relation between the high-velocity flow and the slowly expanding envelope.

2. OBSERVATIONS

The observations were carried out between 2003 February and May, with the five antennas of the partially completed Submillimeter Array (SMA)⁴ at Mauna Kea, Hawaii (Ho et al. 2004). The primary-beam size (HPBW) of the 6 m antennas at 230 and 345 GHz were measured to be $\sim 54''$ and $\sim 36''$, respectively. We obtained the data in two array configurations,

which provided 15 independent baselines. The spectral correlator had a bandwidth of 656 MHz and a frequency resolution of 812.5 kHz.

The visibility data were calibrated using the MIR package (Scoville et al. 1993). We used 1055+018 or 3C 273 as a phase and amplitude calibrator and Callisto as a flux calibrator. The bandpass was calibrated by observations of Jupiter or Saturn. The calibrated visibility data were Fourier-transformed and CLEANed by using the Astronomical Image Processing System with natural weighting. The synthesized beam had a size of 4.4×3.1 with a position angle of -21° at 230 GHz and 2.1×1.9 with a position angle of -28° at 345 GHz. In making maps, we averaged two channels in CO $J = 2-1$ and three channels in CO $J = 3-2$ and made maps with velocity resolution of 2.1 km s^{-1} . The rms noise level of the maps at the velocity resolution of 2.1 km s^{-1} was $0.09 \text{ Jy beam}^{-1}$ (0.15 K in T_B) in CO $J = 2-1$ and 0.3 Jy beam^{-1} (0.77 K in T_B) in CO $J = 3-2$. We averaged the entire 656 MHz of both image sidebands to make maps of the 241 and 335 GHz continuum emission. Continuum maps were made with uniform weighting, which provided a synthesized beam of 3.0×2.2 with a position angle of 37° at 241 GHz and 2.0×1.3 with a position angle of 48° at 335 GHz. The rms noise levels of the 241 and 335 GHz continuum maps were 9 and 20 mJy beam⁻¹, respectively.

3. RESULTS AND DISCUSSION

3.1. Continuum Emission from V Hya

We detected the continuum emission peaks at $\alpha = 10^{\text{h}}51^{\text{m}}37.25^{\text{s}}$, $\delta = -21^\circ15'00''.5$ (J2000.0) at both 241 and 335 GHz. The position of the continuum source coincides well with the stellar position at the observational epoch J2003.25, which is derived from the coordinates and proper motion measured by the *Hipparcos* satellite (Perryman et al. 1997). Figures 1*k* and 1*l* show that the continuum source is not resolved with our beams. This suggests that most of the emission comes from a spatially compact region with a radius of $\leq 1''$ (380 AU). The flux density of the source is $63 \pm 16 \text{ mJy}$ at 241 GHz and $105 \pm 39 \text{ mJy}$ at 335 GHz. The spectral index α between 241

¹ Academia Sinica, Institute of Astronomy and Astrophysics, P.O. Box 23-141, Taipei 106, Taiwan; hirano@asia.sinica.edu.tw.

² Harvard-Smithsonian Center for Astrophysics, 645 North A'ohoku Place, Hilo, HI 96720.

³ Harvard-Smithsonian Center for Astrophysics, 60 Garden Street, Cambridge, MA 02138.

⁴ The Submillimeter Array is a joint project between the Smithsonian Astrophysical Observatory and the Academia Sinica Institute of Astronomy and Astrophysics and is funded by the Smithsonian Institution and the Academia Sinica.

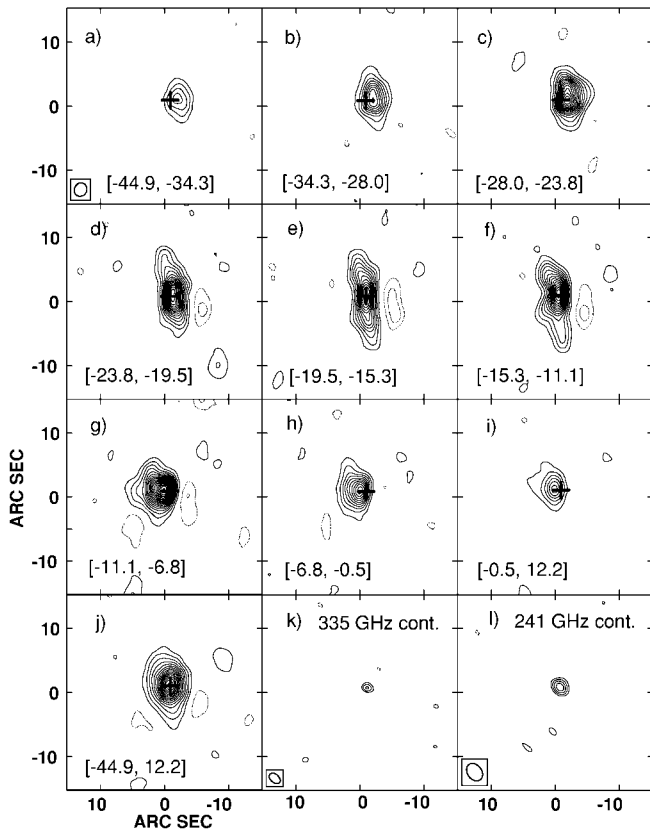


FIG. 1.—(a)–(i) Velocity-channel maps of the CO $J = 3-2$ line. The coordinates of the map center are $\alpha = 10^{\text{h}}51^{\text{m}}37^{\text{s}}.25$, $\delta = -21^{\circ}15'00''.5$ (J2000.0). The velocity range of each panel is shown in brackets. The plus sign denotes the position of the continuum source (see [k], [l]). The contours are drawn every 3σ . The 3σ level of each map is $4.2 \text{ Jy beam}^{-1} \text{ km s}^{-1}$ in (a), $3.3 \text{ Jy beam}^{-1} \text{ km s}^{-1}$ in (b) and (h), $2.7 \text{ Jy beam}^{-1} \text{ km s}^{-1}$ in (c)–(g), and $4.7 \text{ Jy beam}^{-1} \text{ km s}^{-1}$ in (i). (j) Map of CO $J = 3-2$ integrated over the velocity ranges from -44.9 to $+12.2 \text{ km s}^{-1}$. The contours are drawn every 3σ ($13.7 \text{ Jy beam}^{-1} \text{ km s}^{-1}$ step). (k) Map of the 335 GHz continuum emission. The lowest contours are 60 mJy beam^{-1} (3σ) with the step of 20 mJy beam^{-1} (1σ). (l) Map of the 241 GHz continuum emission. The contours are every 9 mJy beam^{-1} (1σ), with the lowest contour at 27 mJy beam^{-1} (3σ).

and 335 GHz is ~ 1.6 , which is shallower than Rayleigh-Jeans. This might imply the contribution of free-free emission from shock-ionized gas close to the star (Luttemoser & Brown 1992; Knapp et al. 1997). However, because of the large uncertainty in the flux at 335 GHz, it is difficult to estimate the contribution of the ionized component to the submillimeter spectra.

If we assume that the continuum emission at 241 and 335 GHz arises from the thermal emission from the dusty envelope, the mass of dust M_{dust} required to produce the observed flux densities is estimated by

$$M_{\text{dust}} \geq \frac{2ap_{\text{dust}}D\lambda^2(S_{\nu} - S_*)}{3Q_{\nu}kT_{\text{dust}}}, \quad (1)$$

in the Rayleigh-Jeans limit. Here S_{ν} is the observed flux, S_* is the flux that comes from the stellar photosphere, and D is the source distance. At 241 GHz, S_* is estimated to be $\sim 10 \text{ mJy}$. We assume that the dust particles have radius a of 2000 \AA , material density ρ_{dust} of 2.25 g cm^{-3} , and emissivity Q_{ν} of 6.17×10^{-4} at 274.6 GHz with a power-law dependence on frequency with index $\beta = 1$. We adopted a grain temperature of 360 K . This corresponds to the grain temperature at $r = 380 \text{ AU}$ if it has a power-law dependence on radius $T_g = T_*(R_*/r)^{2/(4+\beta)}$ (Knapp et al.

1993), with an effective temperature T_* and a radius R_* of the star of 2650 K and $3.8 \times 10^{13} \text{ cm}$ (Knapp et al. 1999), respectively. The mass of dust was calculated to be $6.5 \times 10^{-6} M_{\odot}$. If we assume a constant mass loss, the dust mass-loss rate is estimated to be $5.7 \times 10^{-8} M_{\odot} \text{ yr}^{-1}$ based on an outflow speed of $\sim 16 \text{ km s}^{-1}$ (see § 3.3).

3.2. Flattened Envelope and High-Velocity Bipolar Outflow

Strong CO $J = 2-1$ and $J = 3-2$ emission was detected in the velocity range from $V_{\text{LSR}} = -45$ to $+12 \text{ km s}^{-1}$, corresponding to $\pm \sim 28 \text{ km s}^{-1}$ from the systemic velocity, $V_{\text{sys}} = -17.5 \text{ km s}^{-1}$. Both CO $J = 2-1$ and $3-2$ maps show that the molecular envelope is elongated along the north-south direction. We have smoothed our interferometric maps to mimic the CO $J = 2-1$ and $3-2$ spectra observed with the $30''$ and $20''$ beams, respectively, and compared the spectra observed by Knapp et al. (1997) and Stanek et al. (1995). We found that $\sim 50\%$ of the CO $J = 2-1$ flux and $\sim 35\%$ of the CO $J = 3-2$ flux observed by the single-dish telescope was recovered by the SMA.

The velocity-channel maps of CO $J = 3-2$ emission are shown in Figures 1a–1i. The velocity structure traced by the CO $J = 2-1$ emission is similar to that shown in the CO $J = 3-2$ maps. We found that the approaching part of the envelope is located to the west and the receding part to the east of the star, which is consistent with the previous single-dish CO $J = 2-1$ results of Kahane et al. (1996). The spatial-kinematic structure shown in Figure 1 can be explained if the CO emission arises from an inclined flattened envelope expanding along its radial direction. A flattened disklike structure was also identified by Sahai et al. (2003) on the basis of their interferometric CO $J = 1-0$ observations. However, the observed velocity pattern does not completely match that of a uniformly expanding disk. The largest spatial extents of $\pm 7''$ toward the east and west are shown in the velocity channels of $\pm \sim 8 \text{ km s}^{-1}$ from V_{sys} (Figs. 1g and 1c, respectively) and not in the highest velocity channels. On the other hand, the higher velocity CO emission shown in Figures 1a and 1i comes from the regions close to the central star. The position-velocity diagram of CO $J = 2-1$ along the east-west cut presented in Figure 2b suggests that there are two kinematic components, that is, two vertical ridges at $\Delta V \sim \pm 8 \text{ km s}^{-1}$ from V_{sys} and a horizontal ridge that extends to $\pm 30 \text{ km s}^{-1}$. The $\pm 8 \text{ km s}^{-1}$ components correspond to the two spikes in the CO line profiles observed by Kahane et al. (1996) and Knapp et al. (1997) and are likely to arise from the expanding disk inclined to the line of sight (hereafter referred to as the low-velocity disk). The $\pm 30 \text{ km s}^{-1}$ component has a clear bipolarity with the redshifted part to the east and the blueshifted part to the west (referred to as the medium-velocity wind).

Both CO $J = 2-1$ and $3-2$ lines are associated with the broad wing emission that extends to $\pm \sim 150 \text{ km s}^{-1}$ from V_{sys} . The detection of these wing components is confident because the phases of the visibilities show coherent behavior across the velocity range of $\pm 150 \text{ km s}^{-1}$. In Figures 2a and 2c we show the position-velocity diagrams of the CO $J = 2-1$ along the east-west cut in the blueshifted (ΔV from $V_{\text{sys}} < -40 \text{ km s}^{-1}$) and redshifted ($\Delta V > +40 \text{ km s}^{-1}$) velocity ranges, respectively. In order to improve the signal-to-noise ratio, we made maps of these velocity ranges by averaging 10 channels, providing the effective velocity resolution of 10.6 km s^{-1} . In order to exhibit the features clearly, we smoothed the maps to $5''$ before we created these three position-velocity diagrams.

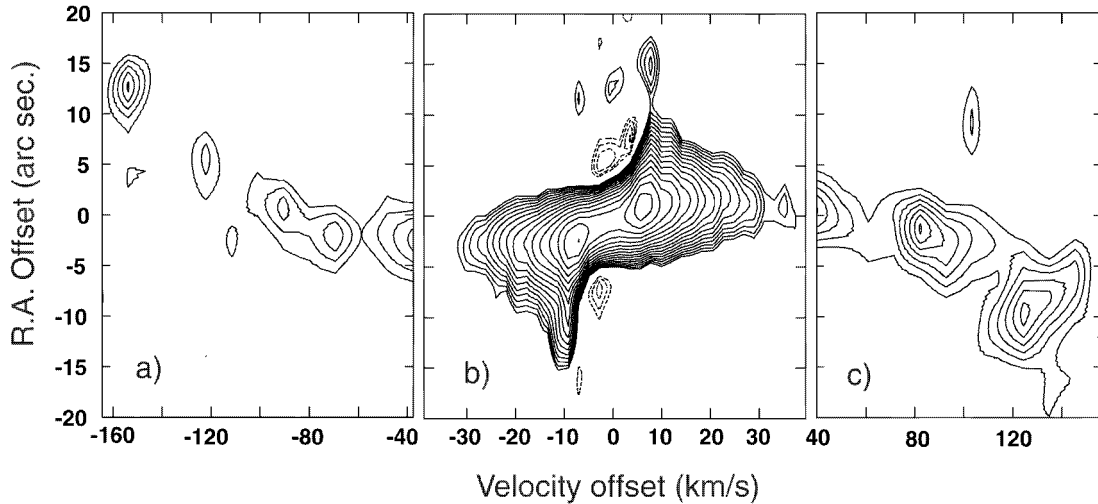


FIG. 2.—Position-velocity map of CO $J = 2-1$ along the east-west cut through the field center in the three different velocity ranges. The effective velocity and spatial resolutions are 10.6 km s^{-1} and $5''$, respectively, in (a) and (c) and 2.1 km s^{-1} and $5''$, respectively, in (b). The contour interval is $0.055 \text{ Jy beam}^{-1}$ (1σ), with the lowest contour at $0.11 \text{ Jy beam}^{-1}$ (2σ) in (a) and (c). The contours in (b) are drawn in a log scale: 0.40, 0.50, 0.63, 0.80, 1.00, 1.3, 1.6, 2.0, 2.5, 3.2, 4.0, 10.0, 12.6, and $15.9 \text{ Jy beam}^{-1}$.

Figures 2a and 2c suggest that emission in the velocity ranges of $\Delta V < \pm 60 \text{ km s}^{-1}$ corresponds to the lower intensity part of the medium-velocity wind. On the other hand, the velocity structure of the higher velocity component with $\Delta V > \pm 60 \text{ km s}^{-1}$ is different. The spatial distribution of the high-velocity component (ΔV from V_{sys} is $\pm 60\text{--}162 \text{ km s}^{-1}$) is shown in Fig-

ure 3 superposed on the intensity-weighted mean velocity map of CO $J = 2-1$. The high-velocity component has its approaching part to the east and the receding part to the west of the star. This orientation is *opposite* that of the lower velocity components as suggested by Knapp et al. (1997). Such an orientation can be explained if the high-velocity component is a pair of collimated jets blown out in the polar direction of the low-velocity jet. Hereafter, we refer to this component as the high-velocity jet. Recently, Sahai et al. (2003) discovered an [S II] emission-line blob with a high negative radial velocity of $\Delta V \sim -240 \text{ km s}^{-1}$ at $0''.2$ east of the central star. This also suggests the presence of a collimated high-velocity jet with an approaching part to the east of the central star. In the CO $J = 2-1$ map, the receding part of the bipolar jet, which has not been observed in [S II] emission probably as a result of the absorption caused by the obscuring disk, is clearly detected to the west of the star. Figures 2a and 2c show that the negative and positive velocities of the high-velocity jet increase as the positional offset from the star increases. Such a velocity increase can be explained if we take into account that the density of the circumstellar envelope decreases rapidly along the east-west direction. Figures 2a, 2c, and 3b show that the high-velocity component consists of discrete clumps separated by $\sim 5''$, suggesting that the high-velocity jet is episodic.

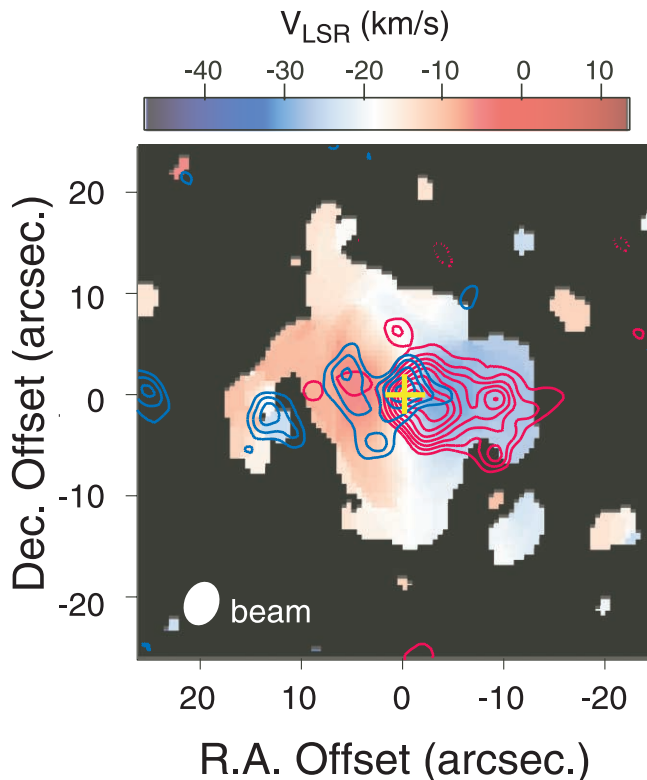


FIG. 3.—CO $J = 2-1$ maps integrated over the velocity range of $\pm 60.0\text{--}162.2 \text{ km s}^{-1}$ from the systemic velocity of -17.5 km s^{-1} (blue and red contours) superposed on the intensity-weighted mean velocity map of CO $J = 2-1$ in the velocity range of $\pm 30 \text{ km s}^{-1}$ from the systemic velocity. The contours are drawn every $14.3 \text{ Jy beam}^{-1} \text{ km s}^{-1}$ (1σ), with the lowest contours at $42.9 \text{ Jy beam}^{-1} \text{ km s}^{-1}$ (3σ).

3.3. Circumstellar Structure of V Hya

The high angular resolution CO $J = 3-2$ and $2-1$ maps suggest that the circumstellar structure of V Hya consists of three kinematic components: the low-velocity disk with radial velocity offsets of $\Delta V = \pm 8 \text{ km s}^{-1}$ from V_{sys} , the medium-velocity wind with $\Delta V < \pm 60 \text{ km s}^{-1}$, and the high-velocity jet with $\Delta V = \pm 60\text{--}160 \text{ km s}^{-1}$. These three components correspond to the $\pm 8 \text{ km s}^{-1}$ spikes, the 45 km s^{-1} wind, and the 200 km s^{-1} wind defined by Knapp et al. (1997), respectively.

The spatial extent of the low-velocity disk along the major (north-south) and minor (east-west) axes measured at the 3σ level are $\pm 8''$ and $\pm 7''$, respectively, in CO $J = 3-2$ and $\pm 15''$ and $\pm 13''$, respectively, in CO $J = 2-1$. If we assume that the disk is thin, the ratio between the major and minor axes suggests that the disk plane is inclined by $\sim 60^\circ$ from the line of sight,

which is consistent with the previous estimation of $\sim 70^\circ$ by Sahai et al. (2003). We find that the gas in the low-velocity disk is moving at an almost constant deprojected velocity of 16 km s^{-1} , which is similar to the typical AGB wind velocity. The north-south extent in the CO $J = 2-1$ map suggests that the low-velocity disk has a radius of 5700 AU and a dynamical timescale of 1700 yr. If we assume that the axis of the high-velocity jet is perpendicular to the disk plane, the deprojected velocity and the dynamical timescale of the jet are estimated to be $70-185 \text{ km s}^{-1}$ and 100–250 yr, respectively.

What is the nature of the medium-velocity wind? Here we present three possible scenarios: (1) the interaction between the low-velocity disk and the high-velocity wind, (2) equatorial mass outflow with higher velocity, and (3) a second bipolar outflow with a different axis. The first case assumes that the dense equatorial disk collimates the spherically expanding or poorly collimated high-velocity wind into the polar direction. In this case, the wind directed to the polar direction can escape rather freely, while the one directed to the equatorial plane pushes the dense molecular gas in the disk plane and produces the medium-velocity wind. The second case is possible if the velocity of the recent mass flow along the equatorial disk plane has been remarkably enhanced for some reason. In either case 1 or case 2, the direction of the medium-velocity wind is close to the disk plane. Therefore, the deprojected velocity of the wind is estimated to be $40-120 \text{ km s}^{-1}$. The dynamical timescale of the medium-velocity wind estimated from the spatial extent of $\sim 5''-8''$, the inclination angle, and the deprojected velocity is 100–400 yr, which is close to the timescale of the high-velocity jet. The third case is the interpretation proposed by Kahane et al. (1996), in which the medium-velocity wind comes from a bipolar outflow with a large opening angle. However, the orientation of the approaching and receding parts of the medium-velocity wind suggests that the axis of this bipolar flow should be close to the plane of the disk. If we take into account the geometry of the low-velocity disk and the high-velocity jet, the case 3 scenario is less likely, although we cannot rule out the possibility that V Hya ejects two orthogonal outflows, as in the case of CRL 2688 (e.g., Cox et al. 2000). In Figure 4, we show a schematic

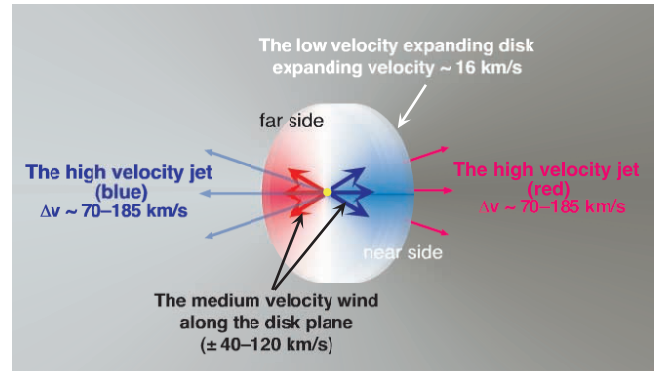


FIG. 4.—Schematic picture of the circumstellar structure of V Hya.

picture of these three kinematic components based on the scenarios of case 1 or 2.

The origin of a disk and jet system like V Hya has not yet been elucidated. However, theoretical models (e.g., Soker 1997; Soker & Rappaport 2000) suggest that it is difficult for a single star to form a flattened disklike structure. The evidence of rapid rotation of V Hya (Barnbaum et al 1995) suggests that this star has a companion. It is likely that the close companion plays an important role in enhancing the equatorial mass loss and producing the disk and jet structure (e.g., Soker 1992; Morris 1987). The circumstellar structure of V Hya resembles that of the proto-planetary nebula CRL 618, which is also associated with large equatorial tori and extremely high-velocity bipolar outflow (Sánchez Contreras & Sahai 2004). The circumstellar structure of V Hya implies that the asymmetric structure with disk and jet appears when the central star is still in the AGB phase.

We wish to thank all the SMA staff in Hawaii, Cambridge, and Taipei for their enthusiastic help during these observations. We also thank P. T. P. Ho, J. M. Moran, and the anonymous referee for helpful comments on the manuscript.

REFERENCES

- Barnbaum, C., Morris, M., & Kahane, C. 1995, *ApJ*, 450, 862
 Cox, P., Lucas, R., Huggins, P. J., Forveille, T., Bachiller, R. Guilleaume, S., Maillard, J. P., & Omont, A. 2000, *A&A*, 353, L25
 Ho, P. T. P., Moran, J. M., & Lo, K. Y. 2004, *ApJ*, 616, L1
 Kahane, C., Audinos, P., Barnbaum, C., & Morris, M. 1996, *A&A*, 314, 871
 Knapp, G. R., Dobrovolsky, S. I., Ivezić, Z., Young, K., Crosas, M., Mattei, J. A., & Rupen, M. P. 1999, *A&A*, 351, 97
 Knapp, G. R., Jorissen, A., & Young, K. 1997, *A&A*, 326, 318
 Knapp, G. R., Sandel, G., & Robson, E. I. 1993, *ApJS*, 88, 173
 Lloyd Evans, T. 1991, *MNRAS*, 248, 479
 Luttermoser, D. G., & Brown, A. 1992, *ApJ*, 384, 634
 Morris, M. 1987, *PASP*, 99, 1115
 Perryman, M. A. C., et al. 1997, *A&A*, 323, L49
 Sahai, R., Morris, M., Knapp, G. R., Young, K., & Barnbaum, C. 2003, *Nature*, 426, 261
 Sahai, R., & Wannier, P. G. 1988, *A&A*, 201, L9
 Sánchez Contreras, C., & Sahai, R. 2004, *ApJ*, 602, 960
 Scoville, N. Z., Carlstrom, J. E., Chandler, C. J., Phillips, J. A., Scott, S. L., Tilanus, R. P. J., & Wang, Z. 1993, *PASP*, 105, 1482
 Soker, N. 1992, *ApJ*, 389, 628
 ———. 1997, *ApJS*, 112, 487
 Soker, N., & Rappaport, S. 2000, *ApJ*, 538, 241
 Stanek, K. Z., Knapp, G. R., Young, K., & Phillips, T. G. 1995, *ApJS*, 100, 169